Available online at www.sciencedirect.com
ScienceDirect
Surface Science 601 (2007) 1574–1581
SURFACE SCIENCE
www.elsevier.com/locate/susc

The Pd(100)-($\sqrt{5} \times \sqrt{5}$)R27°–O surface oxide: A LEED, DFT and STM study

Petr Kostelník [a], Nicola Seriani [b], Georg Kresse [b], Anders Mikkelsen [c], Edvin Lundgren [c], Volker Blum [d], Tomáš Šikola [a], Peter Varga [e], Michael Schmid [e,*]

[a] Institute of Physical Engineering, Brno University of Technology, 616 69 Brno, Czech Republic
[b] Institut für Materialphysik and Centre for Computational Materials Science, Universität Wien, 1090 Wien, Austria
[c] Department of Synchrotron Radiation Research, Institute of Physics, Lund University, Box 118, S-221 00 Lund, Sweden
[d] Fritz-Haber Institut der Max-Planck-Gesellschaft, D-14195 Berlin, Germany
[e] Institut für Allgemeine Physik, Technische Universität Wien, Wiedner Hauptstr. 8-10/134, 1040 Wien, Austria

Received 19 December 2006; accepted for publication 16 January 2007
Available online 25 January 2007

Abstract

Using low energy electron diffraction (LEED), density functional theory (DFT) and scanning tunneling microscopy (STM), we have re-analyzed the Pd(100)-($\sqrt{5} \times \sqrt{5}$)R27°–O surface oxide structure consisting, in the most recent model, of a strained PdO(101) layer on top of the Pd(100) surface [M. Todorova et al., Surf. Sci. 541 (2003) 101]. Both, DFT simulations using the Vienna Ab initio Simulation Package (VASP) and tensor LEED $I(V)$ analysis of newly acquired LEED experimental data, show that the PdO(101) model is essentially correct. However, compared to the previous study, there is a horizontal shift of the PdO(101) layer with respect to the Pd(100) substrate. The atomic coordinates derived by DFT and LEED ($R_P = 0.162$) are in excellent agreement with each other. We also present STM images with atomic resolution showing domain boundaries on the surface oxide and discuss the bonding geometry between the surface oxide and the substrate.

Keywords: Palladium; Oxidation; Low energy electron diffraction (LEED); Density functional calculations; Scanning tunneling microscopy; Low index single crystal surfaces; Surface structure

1. Introduction

Palladium and its surfaces have been in the centre of interest for a long time due to their use in catalytic oxidation of CO and methane. Both metallic and oxidic phases play an important role. For example, Hendriksen et al. [1] have found that the oxidic state has significantly higher activity for CO oxidation, while the opposite had been reported in a previous paper [2]. Also in case of catalytic oxidation of methane by palladium supported on alumina, where the Pd surface can undergo a Pd ↔ PdO transformation during the catalytic process [3], reports do not agree whether metallic Pd with chemisorbed oxygen or oxidic Pd is more active [4,5]. The situation is further complicated by the fact that formation and decomposition of a Pd surface oxide at high temperatures may occur through intermediate phases [6], and by the observation that an inert surface oxide may be highly active at its borders [7] or act as an oxygen reservoir for a reaction occurring on a metallic surface [8]. Considering all these findings, a good knowledge of the structure of the metallic and oxidic phases is needed as a basis for a deeper understanding of the catalytic processes, as well as for future model calculations.

If a Pd(100) surface is exposed to O_2 at elevated temperature under UHV conditions, one can observe up to four different superstructures for O coverages under 1 ML:

* Corresponding author. Tel.: +43 1 58801 13452; fax: +43 1 58801 13499.
E-mail address: schmid@iap.tuwien.ac.at (M. Schmid).

0039-6028/$ - see front matter © 2007 Elsevier B.V. All rights reserved.
doi:10.1016/j.susc.2007.01.026

p(2 × 2), c(2 × 2), p(5 × 5) and $(\sqrt{5} \times \sqrt{5})$R27° [9,10]. The $(\sqrt{5} \times \sqrt{5})$R27° structure occurs at an oxygen coverage of 0.8 ML. The first structural model of Pd(100)-$(\sqrt{5} \times \sqrt{5})$R27°–O, consisting of a PdO(001) layer placed on top of the Pd(100) surface, was proposed by Orent and Bader [9]. This structure was studied by Vu et al. [11] and Saidy et al. [12] using tensor LEED (low energy electron diffraction), giving a best-fit Pendry *R*-factor $R_P = 0.306$. This model had to be dismissed in a study by Todorova et al. [13], introducing a new PdO(101) model determined by density functional theory (DFT), scanning tunneling microscopy (STM), high resolution core level spectroscopy (HRCLS) and preliminary tensor LEED calculations using scanned and digitalized experimental LEED data from Ref. [11]. However no real quantitative LEED study was performed.

In the present work, we focus on confirming and improving the existing PdO(101) model. Using a tensor LEED $I(V)$ analysis of newly acquired experimental data, DFT calculations and STM experiments, we report a detailed study of this surface oxide structure. The structure is shown to be a slightly modified PdO(101) model, differing from Todorova's model by a horizontal shift of the oxide layer with respect to the substrate, leading to a more favorable geometry.

2. Experimental and computational details

The LEED experiments were performed in Vienna using commercial two-grid LEED optics in a mu-metal ultrahigh vacuum (UHV) chamber with base pressure of 10^{-10} Torr. As a substrate, a Pd(100) single crystal was used. The crystal was cleaned by several cycles of sputtering with Ar^+ ions (500 eV, 1.3 μA, 30 min) and subsequent annealing by electron bombardment of the sample holder (900 K, 30 min). Cleanness of the surface was examined by Auger Electron Spectroscopy (AES). There was no contamination by usual impurities (C, O) visible in AES spectra after cleaning and only a sharp diffraction pattern of the (100) surface was visible on the diffraction screen.

The Pd(100)-$(\sqrt{5} \times \sqrt{5})$R27°–O surface was prepared by oxidation of the clean Pd(100) surface in the UHV chamber. The crystal was exposed to O_2 for 15 min at a pressure of 5×10^{-6} Torr at a temperature of 570 K. A sharp $(\sqrt{5} \times \sqrt{5})$R27° pattern was visible on the diffraction screen after cooling down to room temperature.

The LEED $I(V)$ measurements were performed at normal incidence of the electron beam. The LEED patterns starting from 20 up to 350 eV with 2 eV steps were recorded and stored for further analysis. A set of 136 $I(V)$ curves was extracted from these data. The symmetrically equivalent ones were averaged, smoothed and normalized to the primary electron current, giving a set of 19 symmetrically inequivalent $I(V)$ curves (5 integer and 14 fractional) with a total energy range of 3860 eV.

The University of Erlangen TensErLEED program package [14] was used for calculating the theoretical $I(V)$ curves and searching for the best-fit structure. The package uses standard dynamical theory of diffraction and the tensor LEED (TLEED, [15]) perturbation method. In the initial TLEED calculations a program designed by Barbieri and van Hove [16] was used to generate palladium and oxygen phaseshifts with only bulk parameters used in the calculation. The real part of the inner potential was set to $V_{0r} = -10$ eV. For the final steps of the structural refinement, Rundgren's phaseshift program package [17] was used to generate phaseshifts for the already calculated structure, giving a set of nine different phaseshifts (eight for each atom in the first layer and one for palladium atoms in the lower layers and bulk). Phaseshifts up to $l = 10$ were used during the entire calculation. Rundgren's package was also used to calculate the energy dependent real part of the inner potential, giving

$$V_{0r} = \max\left(-9.24, 0.39 - \frac{67.94}{\sqrt{(E/\mathrm{eV}) + 11.57}}\right) \mathrm{eV}. \quad (1)$$

The optimization runs also allowed for a rigid shift of all spectra, with the final result equivalent to a value of V_{0r} about 1.6 eV lower than Eq. (1). The imaginary part of the inner potential was fixed at $V_{0i} = -5i$ eV according to Saidy et al. [12] during the whole calculation. The vibrational amplitude of the bulk Pd atoms was set to 0.122 Å according to the bulk Debye temperature of 274 K. The vibrational amplitude of the oxygen atoms was set to 0.18 Å and further optimized along with the vibrational amplitudes of the palladium atoms in the PdO, Pd2 and Pd3 layers (cf. Fig. 1). For determining the agreement between experimental and theoretical $I(V)$ curves and for the error bars, Pendry's reliability factor R_P and its variation [18] was used. To determine the error bar of a

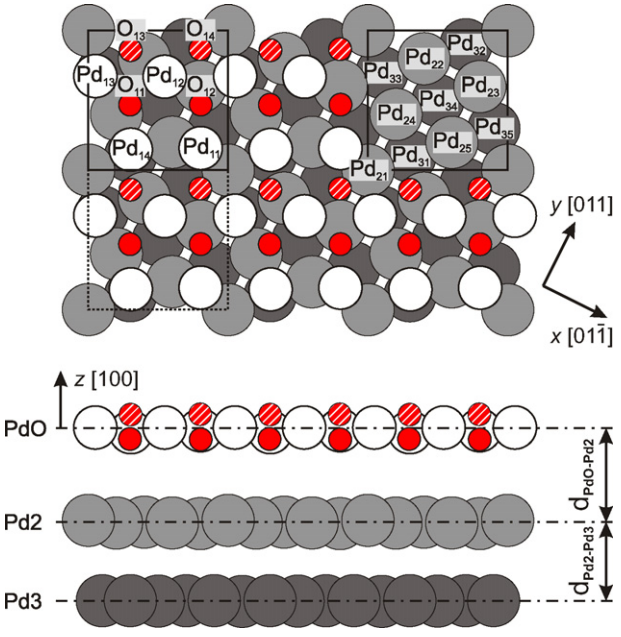

Fig. 1. The model of the Pd(100)-$(\sqrt{5} \times \sqrt{5})$R27°–O structure based on the VASP DFT and tensor LEED analysis. In all figures, small circles are O atoms.

parameter, only this parameter was varied, while the others were fixed at their best-fit value. Re-optimization after variation of one parameter would include coupling between different parameters, but it has been shown that the error bars derived from this more complicated method tend to be overly pessimistic [19].

The STM measurements were performed in Lund using a commercial Omicron STM in an UHV chamber with a base pressure below 1×10^{-10} mbar. The procedure of the $(\sqrt{5} \times \sqrt{5})$R27° structure preparation can be found elsewhere [13]. This preparation procedure, slightly different from the one used for the LEED experiments, resulted in the same structure.

The ab initio calculations were performed with the Vienna Ab initio Simulation Package (VASP) [20], employing the projector-augmented wave method (PAW) [21] as implemented by Kresse and Joubert [22]. The exchange-correlation energy was expressed within the generalized gradient approximation (GGA) in the formulation of Perdew et al. [23] commonly referred to as PW91. The surface was modeled by a slab of four Pd layers for the simulated annealing and by 8 Pd layers, four of which were fully relaxed, in the relaxation and all further analysis. An energy cutoff of 250 eV was employed for the simulated annealing and the structural optimization, raised to 300 eV for the simulation of STM images and the calculation of core level shifts (CLS). Brillouin zone integration was performed on a Monkhorst–Pack $(2 \times 2 \times 1)$ grid for the simulated annealing and an $(8 \times 8 \times 1)$ grid for the relaxation. We used the theoretical lattice constant of 3.95 Å for bulk Pd, which is slightly larger than the experimental value of 3.89 Å. Simulated annealing [24] was performed starting from a temperature of 3000 K and cooling to 500 K in 25 ps. Relaxation was performed by damped molecular dynamics until the forces on the atoms became smaller than 0.002 eV/Å.

3. Results and discussion

3.1. DFT results

Simulated annealing was performed starting from a configuration with Pd atoms coordinated to three or four oxygen atoms, unrelated to the structure proposed in Ref. [13]. During annealing, the oxide monolayer underwent a structural change and already at a temperature of 2000 K the ordering with two types of Pd atoms, coordinated by two and four O atoms, respectively, was clearly visible. In the following, we will simply refer to these as twofold and fourfold Pd. The resulting structure was then relaxed; structural data are reported in Tables 1 and 2. We have also performed a structural relaxation with the structure described in Ref. [13] as a starting point, again leading to the same structure as obtained by simulated annealing. To achieve sufficient accuracy for comparison with the LEED experiment, it was necessary to require the residual forces to be smaller than 0.002 eV/Å. After relaxing with a less stringent convergence criterion of 0.02 eV/Å for the atomic forces, some atomic coordinates differed from those of the final minimum by as much as 0.1 Å, indicating a very shallow potential energy surface. In the relaxed structure the Pd atoms lie neither exactly in the hollow site nor ex-

Table 1
Optimized vertical parameters and the LEED vibrational amplitudes of the Pd(100)-$(\sqrt{5} \times \sqrt{5})$R27°–O structure

Atom	VASP DFT	TLEED	
	Δz (Å)	Δz (Å)	A_{vib} (Å)
Pd_{11}	−0.050	−0.039 ± 0.043	0.175 ± 0.042
Pd_{12}	0.085	0.081 ± 0.035	
Pd_{13}	0.083	0.081 ± 0.047	
Pd_{14}	−0.118	−0.124 ± 0.046	
O_{11}	−0.424	−0.424 ± 0.078	0.215 ± 0.084
O_{12}	−0.426	−0.444 ± 0.075	
O_{13}	0.617	0.651 ± 0.052	
O_{14}	0.634	0.666 ± 0.053	
$d_{PdO–Pd2}$	2.374	2.336 ± 0.030	
Pd_{21}	0.078	0.092 ± 0.054	0.160 ± 0.066
Pd_{22}	−0.024	0.012 ± 0.061	
Pd_{23}	−0.002	−0.053 ± 0.064	
Pd_{24}	−0.021	−0.028 ± 0.055	
Pd_{25}	−0.030	−0.023 ± 0.061	
$d_{Pd2–Pd3}$	1.959	1.961 ± 0.028	
Pd_{31}	−0.019	−0.012 ± 0.042	0.129 ± 0.061
Pd_{32}	0.014	−0.007 ± 0.060	
Pd_{33}	0.005	0.023 ± 0.051	
Pd_{34}	−0.021	0.008 ± 0.076	
Pd_{35}	0.021	−0.012 ± 0.050	
$d_{Pd3–Pd_{bulk}}$	1.965	1.952 ± 0.029	

All interlayer distances are given with respect to the center of mass of the respective atomic layer taking only the Pd atoms into account. The DFT coordinates are rescaled by −1.6% to comply with the experimental lattice constant.

Table 2
Optimized in-plane coordinates of the structure

Atom	VASP DFT		TLEED	
	x (Å)	y (Å)	x (Å)	y (Å)
Pd_{11}	3.920	3.035	3.980 ± 0.113	3.080 ± 0.149
Pd_{12}	1.108	5.153	1.155 ± 0.114	5.185 ± 0.137
Pd_{13}	−1.648	3.805	−1.585 ± 0.124	3.845 ± 0.118
Pd_{14}	1.166	1.602	1.270 ± 0.124	1.635 ± 0.135
O_{11}	0.264	3.352	0.345 ± 0.184	3.400 ± 0.192
O_{12}	3.035	4.777	3.125 ± 0.170	4.795 ± 0.195
O_{13}	−0.773	5.516	−0.710 ± 0.170	5.560 ± 0.189
O_{14}	1.947	6.904	2.010 ± 0.145	6.975 ± 0.184
Pd_{21}	−0.004	−0.012	0.000 ± 0.122	−0.050 ± 0.129
Pd_{22}	−0.052	5.552	−0.075 ± 0.117	5.535 ± 0.142
Pd_{23}	2.723	5.475	2.705 ± 0.132	5.535 ± 0.122
Pd_{24}	0.010	2.762	0.020 ± 0.159	2.735 ± 0.118
Pd_{25}	2.727	2.695	2.750 ± 0.155	2.695 ± 0.143
Pd_{31}	1.372	1.380	1.375*	1.375*
Pd_{32}	1.410	6.864	1.375*	6.877*
Pd_{33}	−1.383	4.126	−1.375*	4.126*
Pd_{34}	1.377	4.137	1.375*	4.126*
Pd_{35}	4.146	4.119	4.126*	4.126*

The base vectors of the $(\sqrt{5} \times \sqrt{5})$R27° cell are $\mathbf{a}_1 = (5.502, 2.751)$ Å and $\mathbf{a}_2 = (-2.751, 5.502)$ Å. The asterisk (*) indicates coordinates not varied in the LEED structural search. The DFT coordinates are rescaled to the experimental lattice constant.

actly at the bridge position, contrary to what was suggested in Ref. [13].

Similar to the model in Ref. [13], two O atoms (O_{13} and O_{14} in Fig. 1, referred to as O_{up}) are about 0.6 Å above the Pd atoms in the oxide layer, the other two ≈0.4 Å below (O_{down}). The fourfold Pd atoms, Pd_{12} and Pd_{13}, are slightly higher than the twofold Pd atoms and have an almost planar coordination to the surrounding O atoms (sum of O–Pd–O angles equals 360°), with two different sets of O–Pd–O angles: ≈100° for O_{up}–Pd–O_{up} and O_{down}–Pd–O_{down}, and ≈80° for the O_{up}–Pd–O_{down} angles. For the twofold Pd atoms, due to their lower height, the geometry deviates from linearity with an O–Pd–O angle of ≈170°.

Re-calculating the previously measured core level shifts [13] using the procedure described in Ref. [25] confirms the modification of the model. The calculated core level shifts using the present model as well as the experimental values from Ref. [13] are shown in Table 3. For the Pd2 atoms in the uppermost substrate layer, forming the interface to the surface oxide, we find a significant improvement. In contrast to the previous model, the new model with its shifted oxide overlayer shows a much better fit to the negative core level shifts observed experimentally. Obviously, the small positive shifts of the Pd_{23} and Pd_{24} atoms were not resolved experimentally due to their proximity to the bulk signal and the peaks of the twofold Pd_{11} and Pd_{14} atoms. For the twofold and fourfold coordinated Pd atoms in the surface oxide, some modest improvements of the agreement between the calculated and experimental shifts can be seen. All together, our refined model leads to an improved agreement of the core level shifts.

3.2. Tensor LEED results

Two possible structural models were chosen as the starting coordinates for the tensor LEED search: the structure derived from the paper by Todorova et al. [13] and a structure resulting from the VASP DFT calculation. In the first TLEED search cycle (reference calculation, delta calculation, search for the best-fit structure), the vertical displacements in the PdO, Pd2 and Pd3 layers were varied, as well as vibrational amplitudes for these layers (equal amplitude of all atoms within a layer, but separate values for Pd and O in the PdO layer). The in-plane positions remained fixed. This results in 18 independent structural parameters and four nonstructural parameters, and an experimental data range of 175 eV per free parameter. With the model by Todorova et al., the Pendry R-factor reached $R_P = 0.56$. This is significantly higher than the best-fit value $R_P = 0.28$ reported in Ref. [13]. We attribute much of this difference to the much larger energy range used in our study, compared to Ref. [13]. In addition, scanning and digitization of the LEED spectra used in Ref. [13] may have caused some degradation of the data. Finally, in the LEED analysis of Ref. [13], large buckling amplitudes in the Pd3 layer were found, to which the R-factor showed little sensitivity, and which are also at odds with the present first-principles results. These buckling values are probably an artifact related to the shifted in-plane positions, which were not varied in the LEED study in Ref. [13]. Starting from the VASP DFT structure, $R_P = 0.28$ was reached. Also when applying only horizontal variations to the atoms of the PdO(1 0 1) layer of Todorova's model, the R-factor reached $R_P = 0.49$, giving a clear indication that a horizontal shift of the PdO(1 0 1) layer is needed to give a reasonable agreement. Hence, for the structural refinement, the coordinates resembling the new VASP DFT based model of the structure were used as a starting point.

In the following calculations we decided to optimize the in-plane coordinates of the PdO layer along with the vertical coordinates and layer-wise vibrational amplitudes of the atoms of the first three atomic layers PdO, Pd2 and Pd3 (all other parameters were kept at the bulk values), resulting in 34 independent structural parameters and four independent nonstructural parameters, giving approximately 102 eV range for each parameter, which is still very good for a LEED $I(V)$ analysis. This resulted in a best-fit structure with an overall R-factor of $R_P = 0.219$. At this point Rundgren's package was used to calculate new phaseshifts and the energy-dependent real part of the inner potential using these optimized structural parameters as input. With these new values, the structural optimization resulted in a structure very close to the final one with an overall R factor of $R_P = 0.175$. After that we tried to use the DFT-calculated in-plane coordinates for the Pd2 layer in the LEED model. This resulted in an immediate decrease of the R-factor to $R_P = 0.167$, indicating that in-plane displacements of the substrate atoms should be varied. After including the Pd2 in-plane coordinates as free parameters in the structural analysis, the search reached its final minimum of $R_P = 0.162$ (0.129 for the integer beams, 0.174 for the fractional beams; see Fig. 2). This brings 10 new independent structural parameters to the search, resulting in an 80 eV range per parameter, still acceptable for a LEED $I(V)$ analysis.

The R factor could be further improved to $R_P = 0.154$ by variation of the in-plane coordinates of the Pd3 layer,

Table 3
Core level shifts for the 3d states of the Pd atoms in the oxide monolayer and in the first metallic layer: initial-state contributions (i.e. core level shifts calculated without relaxation of the other electronic states) and total core level shifts

	Initial states	Total CLS	Experimental values (Ref. [13])
Pd_{11}	+0.18	+0.32	+0.38
Pd_{12}	+0.88	+1.06	+1.30
Pd_{13}	+0.80	+1.07	+1.30
Pd_{14}	+0.15	+0.42	+0.38
Pd_{21}	−0.38	−0.24	−0.32
Pd_{22}	−0.38	−0.26	−0.32
Pd_{23}	+0.07	+0.10	
Pd_{24}	+0.17	+0.16	
Pd_{25}	−0.27	−0.17	−0.32

A Pd atom in the fourth metallic layer was taken as bulk reference.

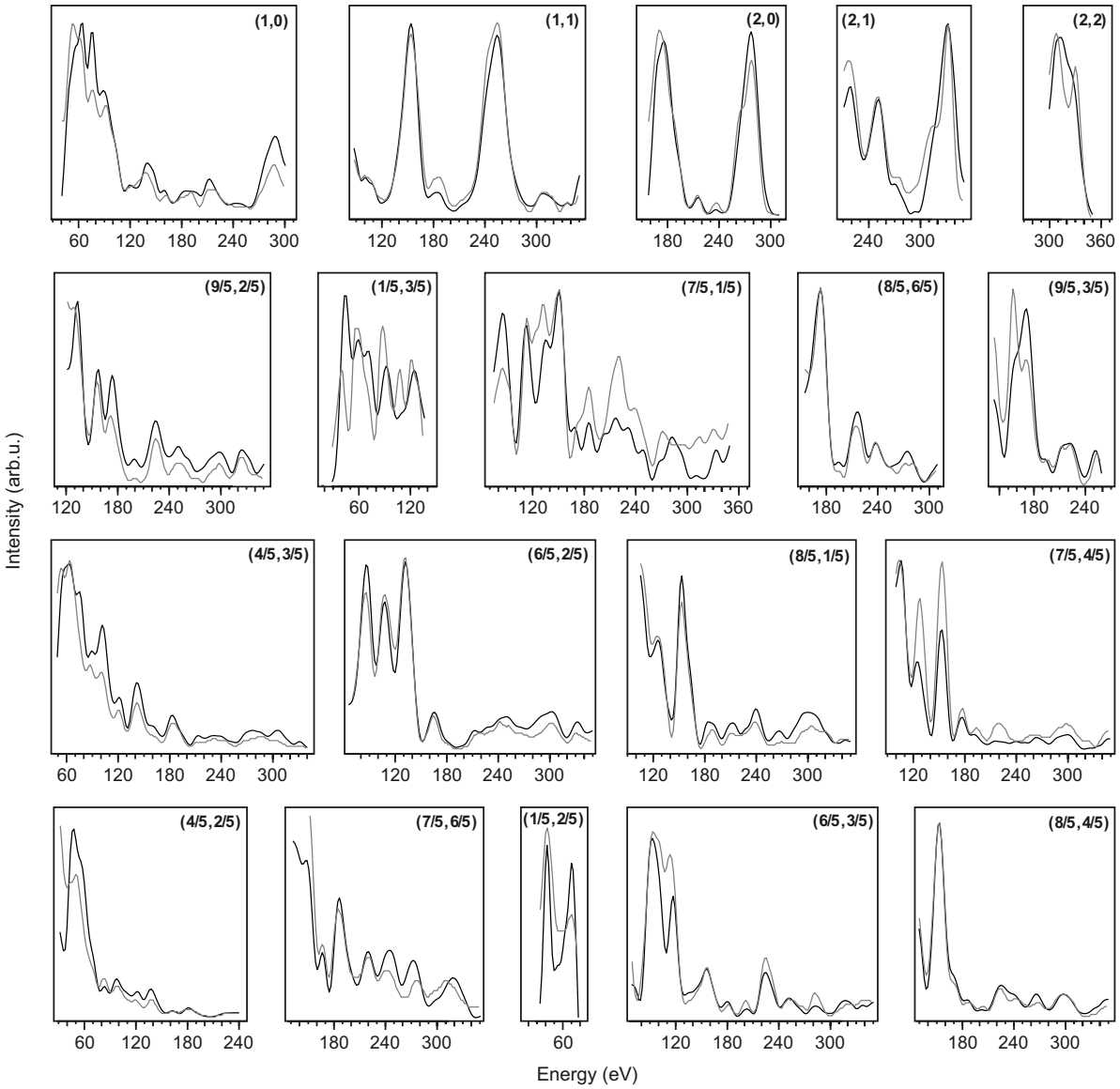

Fig. 2. Comparison of the measured (black) and calculated (grey) $I(V)$ curves of the best-fit model of the Pd(1 0 0)-($\sqrt{5} \times \sqrt{5}$)R27°–O structure ($R_P = 0.162$).

but this leads to Pd3 in-plane shifts unrelated to the DFT coordinates and the LEED error bars are much larger than the relaxations calculated by DFT. Furthermore, the energy range per parameter decreases to only 66 eV. All this indicates that the variation of the Pd3 in-plane coordinates is over-fitting and we therefore present the LEED data with the in-plane displacements of the oxide and the first substrate layer (Pd2), keeping the in-plane coordinates of the Pd3 layer at the bulk values. The excellent agreement of the DFT and LEED coordinates (see Tables 1 and 2) leads us to the conclusion that the model is correct.

3.3. Experimental and calculated STM images

The STM images (Figs. 3a and 4a) show a structure where one can identify three different atomic types: the first one forms rows of bright atoms blending into each other, while the second and third form rows of alternating bright and dark atoms; the dark atoms sometimes appear as holes. We have also calculated an STM image (Fig. 3b) for the same tunneling voltage, employing the Tersoff–Hamann approximation [26]. Comparison of the experimental and calculated STM image shows that the bright rows consist of twofold O-coordinated Pd atoms, which appear with almost the same apparent height. According to the simulated STM image, the other two Pd atoms in the unit cell, appearing bright and dark in alternation, must be identified as fourfold Pd atoms. Identifying the bright smeared-out rows as Pd with two O neighbors and the Pd atoms appearing individually and with varying height as fourfold Pd is in agreement with the appearance of the twofold and fourfold Pd in the surface oxide on Pd(1 1 1) [27]. This appearance can be rationalized by assuming that the O atoms appear as dark depressions in the STM images (like on most metal

surfaces for low oxygen coverage). Thus, the fourfold Pd atoms have four depressions around them, making them stand out as individual atoms. The rows of twofold Pd atoms are only flanked by O rows, while no dark O atoms separate the twofold Pd atoms from each other, thus the twofold Pd atoms do not appear well-separated in the STM images. Our assignment of the twofold and fourfold Pd atoms is different from that made in the work of Todorova et al. [13], where the rows of equally bright atoms were attributed to the fourfold atoms.

Interestingly, the two fourfold Pd atoms, Pd_{12} and Pd_{13}, appear with significantly different height (in the experimental STM images, Pd_{12} appears about 0.3 Å higher than Pd_{13}), although they are geometrically at the same height according to both DFT and LEED (Table 1). Therefore, their different appearance is an electronic effect. Indeed, DFT shows that the density of states projected onto the s, p_z and d_{z^2} atomic orbitals (those contributing to the tunneling current above an atom) is significantly higher for Pd_{12} than for Pd_{13} between E_F and $E_F + 0.4$ eV. The different appearance of the two atoms can be also understood on more qualitative grounds. The "dark" Pd_{13} atom is positioned near a hollow site of the substrate; its shortest bond length to the substrate (Pd_{13}–Pd_{23}) is 2.90 Å and thus significantly larger than the Pd–Pd distance in bulk Pd (2.75 Å). This means that Pd_{13} binds only weakly to the substrate, providing no good channel for the tunneling electrons to flow to the bulk. The "bright" Pd_{12} atom, which is near a bridge site, has two significantly shorter bonds to the substrate (Pd_{12}–Pd_{22}: 2.75 Å; all bond lengths based on DFT and scaled to the experimental lattice constant). This effect of the apparent height increasing from hollow via bridge to on-top positions of the substrate was also observed for the surface oxide on Rh(1 1 1) [28]. The two twofold Pd atoms, Pd_{11} and Pd_{14}, appear with slightly different height in the calculated STM image, reflecting their slightly different geometric height, while their apparent height in the experimental images is almost equal, in spite of their different sites on the substrate.

The calculated STM image also shows indications of the upper O atoms being visible as small protrusions (O_{13} and O_{14}; small hatched circles in Fig. 3b). Calculated STM images for lower tunneling voltages (not shown) have protrusions only at the sites of the Pd atoms. Since the details of the experimental STM images depend on the state of the tip and the images chosen show the Pd atoms more distinctly than the simulated image, we consider it likely that the appearance of our experimental images (and the apparent absence of the O_{up} atoms) is also influenced by the interaction of the tip with the surface, not accounted for in the Tersoff–Hamann approach.

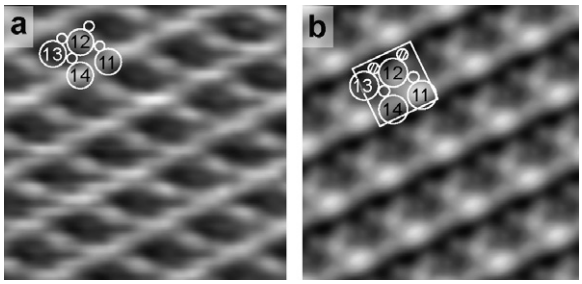

Fig. 3. STM images: (a) experimental ($V_{sample} = +0.76$ V, $I_t = 0.57$ nA) and (b) simulated (states between the Fermi energy E_F and $E_F + 0.6$ eV). In one unit cell, the Pd atoms are labelled by their numbers; identification is based on the simulated image (b) showing that the twofold Pd_{11} and Pd_{14} atoms appear as bright rows and the fourfold Pd_{12} appears higher than Pd_{13}. Small circles indicate oxygen atoms. The upper O atoms O_{13} and O_{14} are hatched in (b).

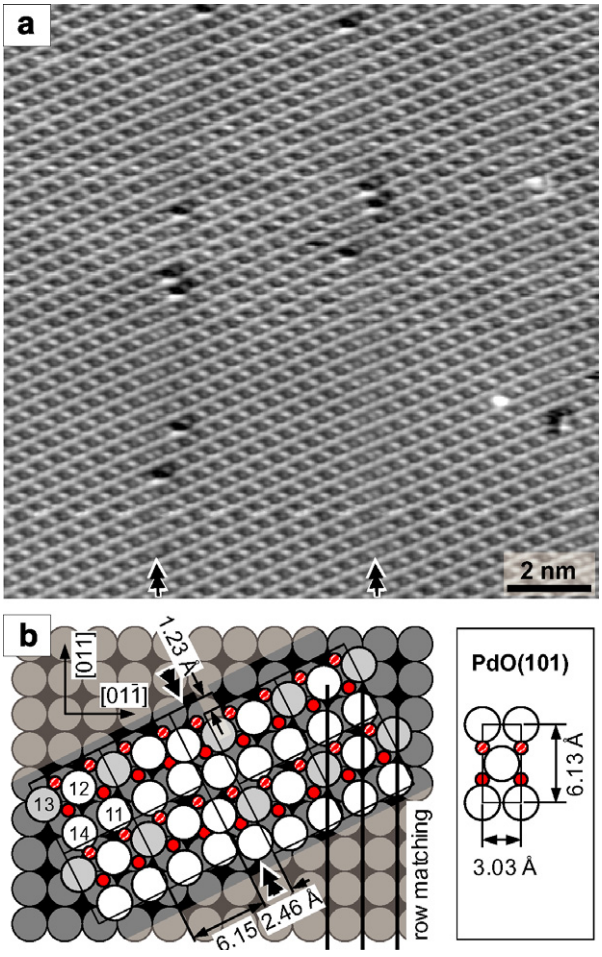

Fig. 4. (a) STM image (+0.59 V, 0.85 nA) of the $(\sqrt{5} \times \sqrt{5})$ structure. (b) Schematic model of a domain boundary. The Pd_{11}–Pd_{14} atoms are labelled by their numbers at the left. The PdO(1 0 1) unit cell is shown for comparison. Domain boundaries are indicated by double arrows in (a) and (b).

3.4. Domain boundaries

STM images of the $(\sqrt{5} \times \sqrt{5})$ structure show a fairly regular array of stripes, where the contrast between dark Pd_{13} and bright Pd_{12} atoms vanishes (marked by double arrows in Fig. 4a). A closer examination shows that these stripes are domain boundaries between different translational domains of the reconstruction. A schematic model

of such a domain boundary is shown in Fig. 4b. At the right side of the domain boundary, the unit cells are shifted by 1/2 [0 1 $\bar{1}$]. At the boundary, atoms are inserted to fill the gap, leaving the rows of Pd atoms with twofold and those with fourfold coordination by oxygen intact. The domain boundary leads to a slight wiggling of these rows, both visible in the STM image and marked as a 1.23 Å shift in the schematic model.

As the model in Fig. 4b shows, compared to the undisturbed $(\sqrt{5} \times \sqrt{5})$ reconstruction, the domain boundary leads to a shorter average distance of the atoms in the direction of the twofold and fourfold O-coordinated Pd rows of the surface oxide. Whereas the average interatomic distance along these rows in the ideal $(\sqrt{5} \times \sqrt{5})$ structure is 6.15/2 Å = 3.08 Å, in the domain boundary one atom is inserted on 2.46 Å space (neglecting the sidewards movement of the rows). The STM images show that the interatomic distances are distributed more evenly, however. With an average distance between the domain boundaries of approx. ten $(\sqrt{5} \times \sqrt{5})$ units, an average interatomic distance of 3.04–3.05 Å along the rows of the surface oxide is found.

Comparison with the (1 0 1) surface unit cell of PdO (Fig. 4b) tells us that this shorter interatomic distance explains the formation of the domain boundaries. The long side of the PdO(1 0 1) unit cell has a length of 6.13 Å, which is well matched by the size of the $(\sqrt{5} \times \sqrt{5})$ surface oxide cell (6.15 Å). The short side of the PdO(1 0 1) cell is 3.03 Å long; this value is equal to the Pd–Pd and O–O distances in that direction. This distance is shorter than the respective distance in an unperturbed $(\sqrt{5} \times \sqrt{5})$ structure, which is 3.08 Å, as mentioned previously. Thus, a perfect $(\sqrt{5} \times \sqrt{5})$ surface oxide is under tensile stress, which is relieved by the formation of the domain boundaries.

The model of the domain boundary (Fig. 4b) also shows that the "row matching" between the surface oxide and substrate is conserved at the domain boundaries, i.e., all Pd atoms of the surface oxide are still close to the [0 1 1]-oriented rows of hollow and bridge sites of the substrate, avoiding the on-top sites. This row matching also avoids placing O_{down} atoms too close to unfavorable hollow sites. The slight wiggles in the oxide (1.23 Å sidewards displacement in Fig. 4b) can be seen as a direct consequence of the row matching, as such a distortion of the surface oxide would not occur without the row-matching constraint imposed by the substrate.

3.5. Discussion

A comparison of the old [13] and new model (Fig. 5) reveals that there is a shift of the PdO(1 0 1) layer with respect to the substrate. The reason for this shift can be found in the binding preferences of the surface atoms. In surface oxides, the oxygen atoms binding with the substrate prefer the on-top sites of the substrate [27–30]. In our case, this applies to the lower oxygen atoms O_{11} and O_{12}. The palladium atoms prefer the hollow sites of the substrate and

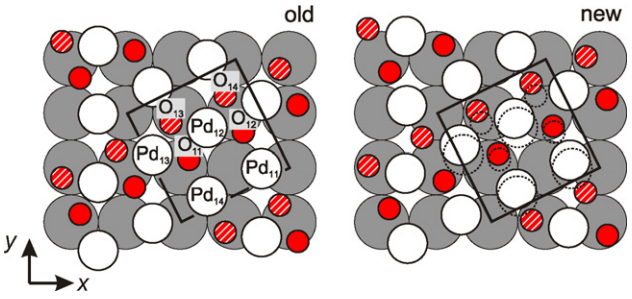

Fig. 5. Comparison of the old [13] and new proposed model. In the new model, the atomic positions of the old model are indicated as dotted circles.

strictly avoid on-top sites. As mentioned previously, this is accomplished by the "row matching" between the hollow-bridge sites of the substrate and the Pd atoms in the oxide, constraining the positions of the oxide in the [0 1 $\bar{1}$] direction (x). Moving the oxide along [0 1 1] (the y direction) does not lead to big changes with respect to the Pd atoms (some gain energy by moving into a hollow site, some lose it by moving closer to a bridge site). A movement along y away from the optimum position will break the bond between one of the lower O atoms and its nearest substrate Pd atom, however. With bond lengths of 2.05 and 2.07 Å (based on scaled DFT coordinates), these bonds have almost the same strength as those within the surface oxide layer (1.90–2.05 Å). Thus, concerning the position with respect to the substrate, in spite of their different structure, the surface oxides on Pd(1 1 1) and Pd(1 0 0) follow the same rules, trying to get the lower O atoms (O_{down}) into on-top sites and the Pd atoms into hollows, and both structures achieve this by row matching in one direction.

Comparing our model to that of Todorova et al. (Fig. 5), the overlayer moves mainly in y direction, thus it directly affects the bonding of the lower O atoms. Obviously, in the previous model, the O_{12} atom was too far from the underlying Pd substrate atom (Pd_{23}), weakening this bond and resulting in a structure that is slightly less favorable than the refined model.

With respect to bond lengths, the surface oxide follows the usual rule that (surface) oxides of the 4d transition metals have metal-oxygen bonds around 2 Å. As mentioned previously, the O–O distances along the rows are ≈3.05 Å and also typical for these oxides. The O–O distances in the other direction (O_{11}–O_{13} and O_{12}–O_{14}) are rather short, however (2.61 Å), even slightly below the short O–O distance in bulk PdO (2.66 Å).

Finally, we should mention that the excellent agreement between the LEED and DFT coordinates obtained in our study provides another confirmation of the high accuracy of these methods, also adding confidence to those DFT studies where the cell is too large for quantitative LEED. There is a caveat, however, in that the DFT studies must be sufficiently well converged. In case of a shallow potential energy surface like ours, for sufficient accuracy it was required that the residual forces must be below 0.002 eV/Å,

which is far more stringent than the usual criterion of forces below 0.01 or 0.02 eV/Å.

4. Conclusions

We have shown that the previously proposed PdO(1 0 1) model of the Pd(1 0 0)-($\sqrt{5} \times \sqrt{5}$)R27°–O surface oxide structure is essentially correct, but an in-plane shift of the PdO(1 0 1) layer is needed to reach good agreement with the LEED data. The same conclusion was obtained by the new DFT calculations of the structural model, and excellent agreement between LEED and DFT was found. We have also presented a new interpretation of the STM images consistent with DFT and previous studies of the Pd(1 1 1) surface oxide.

Acknowledgements

This project was supported by the Austrian Fonds zur Förderung der wissenschaftlichen Forschung, the Czech-Austrian project KONTAKT ME 2004-15 and the European Union under Contract No. NMP3-CT-2003-505670 (NANO2), the Swedish Research Council, the Crafoord foundation and the Knut and Alice Wallenberg foundation.

References

[1] B.L.M. Hendriksen, S.C. Bobaru, J.W.M. Frenken, Surf. Sci 552 (2004) 229.
[2] G. Zheng, E.I. Altman, J. Phys. Chem. B 106 (2002) 1048.
[3] A.K. Datye, J. Bravo, T.R. Nelson, P. Atanasova, M. Lyubovsky, L. Pfefferle, Appl. Catal. A: Gen. 198 (2000) 179.
[4] M. Lyubovsky, L. Pfefferle, Catal. Today 47 (1999) 29.
[5] J.G. McCarthy, Catal. Today 26 (1995) 283.
[6] H. Gabasch, W. Unterberger, K. Hayek, B. Klötzer, G. Kresse, C. Klein, M. Schmid, P. Varga, Surf. Sci. 600 (2006) 205.
[7] J. Klikovits, M. Schmid, J. Gustafson, A. Mikkelsen, A. Resta, E. Lundgren, J.N. Andersen, P. Varga, J. Phys. Chem. B 110 (2006) 9966.
[8] E. Lundgren, J. Gustafson, A. Resta, J. Weissenrieder, A. Mikkelsen, J.N. Andersen, L. Köhler, G. Kresse, J. Klikovits, A. Biedermann, M. Schmid, P. Varga, J. Electron. Spectrosc. Relat. Phenom. 144–147 (2005) 367.
[9] T.W. Orent, S.D. Bader, Surf. Sci. 115 (1982) 323.
[10] G. Zheng, E.I. Altman, Surf. Sci. 504 (2002) 253.
[11] D.T. Vu, K.A.R. Mitchell, O.L. Warren, P.A. Thiel, Surf. Sci. 318 (1994) 129.
[12] M. Saidy, O.L. Warren, P.A. Thiel, K.A.R. Mitchell, Surf. Sci. 494 (2001) L799.
[13] M. Todorova, E. Lundgren, V. Blum, A. Mikkelsen, S. Gray, J. Gustavson, M. Borg, J. Rogal, K. Reuter, J.N. Andersen, M. Scheffler, Surf. Sci. 541 (2003) 101.
[14] V. Blum, K. Heinz, Comput. Phys. Commun. 134 (2001) 392.
[15] R.J. Rous, J.B. Pendry, Surf. Sci. 219 (1989) 355.
[16] A. Barbieri, M.A. Van Hove, private communication, 2003.
[17] J. Rundgren, Phys. Rev. B 68 (2003) 125405.
[18] J.B. Pendry, J. Phys. C 13 (1980) 937.
[19] M. Sporn, E. Platzgummer, S. Forsthuber, M. Schmid, W. Hofer, P. Varga, Surf. Sci. 416 (1998) 423.
[20] G. Kresse, J. Furthmüller, Comput. Mater. Sci. 6 (1996) 15.
[21] P.E. Blöchl, Phys. Rev. B 50 (1994) 17953.
[22] G. Kresse, D. Joubert, Phys. Rev. B 59 (1999) 1758.
[23] J.P. Perdew, J.A. Chevary, S.H. Vosko, K.A. Jackson, M.R. Pederson, D.J. Singh, C. Fiolhais, Phys. Rev. B 46 (1991) 6671.
[24] G. Kresse, W. Bergermayer, R. Podloucky, E. Lundgren, R. Koller, M. Schmid, P. Varga, Appl. Phys. A 76 (2003) 701.
[25] L. Köhler, G. Kresse, Phys. Rev. B 70 (2004) 165405.
[26] J. Tersoff, D.R. Hamann, Phys. Rev. B 31 (1985) 805.
[27] E. Lundgren, G. Kresse, C. Klein, M. Borg, J.N. Andersen, M. De Santis, Y. Gauthier, C. Konvicka, M. Schmid, P. Varga, Phys Rev. Lett. 88 (2002) 246103.
[28] J. Gustafson, A. Mikkelsen, M. Borg, E. Lundgren, L. Köhler, G. Kresse, M. Schmid, P. Varga, J. Yuhara, X. Torrelles, C. Quirós, J.N. Andersen, Phys. Rev. Lett. 92 (2004) 126102.
[29] E. Lundgren, A. Mikkelsen, J.N. Andersen, G. Kresse, M. Schmid, P. Varga, J. Phys. Condens. Matter. 18 (2006) R481.
[30] J. Gustafson, A. Mikkelsen, M. Borg, J.N. Andersen, E. Lundgren, C. Klein, W. Hofer, M. Schmid, P. Varga, L. Köhler, G. Kresse, N. Kasper, A. Stierle, H. Dosch, Phys. Rev. B 71 (2005) 115442.